

Identification of a functional point defect in SrTiO_3

Daesu Lee,¹ Hongwei Wang,² Brenton A. Noesges,³ Thaddeus J. Asel,³ Jinbo Pan,² Jung-Woo Lee,¹ Qimin Yan,² Leonard J. Brillson,³ Xifan Wu,² and Chang-Beom Eom^{1,*}

¹Department of Materials Science and Engineering, University of Wisconsin–Madison, Madison, Wisconsin 53706, USA

²Department of Physics, Temple University, Philadelphia, Pennsylvania 19122, USA

³Department of Electrical and Computer Engineering and Department of Physics, The Ohio State University, Columbus, Ohio 43210, USA



(Received 5 October 2017; revised manuscript received 13 March 2018; published 21 June 2018)

Unveiling both the presence and nature of point defects is one of the biggest challenges in condensed matter physics and materials science. Particularly in complex oxides, even a minute amount of unavoidable point defects could generate novel physical phenomena and functions, such as visible light emission and ferroelectricity, yet it remains elusive to clearly identify such point defects. Here, taking SrTiO_3 as a model system, we show that iterative feedback among atomic-layer- and stoichiometry-controlled thin-film epitaxy, hybrid density functional theory, and high-resolution cathodoluminescence spectroscopy allows for the identification of a functional cationic defect, the Ti antisite (Ti_{Sr}) defect. Our cathodoluminescence measurements reveal sub-band-gap luminescence, whose spectral fine structures show excellent quantitative agreement, as well as a one-to-one correspondence, with the theoretically predicted optical transitions from intrinsic point defects such as Ti_{Sr} . Guided by the theory and spectroscopic results, we also control a cation stoichiometry, and it in turn results in good systematics in cathodoluminescence spectra. Not limited to the identification of Ti_{Sr} , this approach allows for more reliable, self-consistent defect study, and provides critical insight into a microscopic picture of point defects in complex oxides.

DOI: 10.1103/PhysRevMaterials.2.060403

I. INTRODUCTION

Point defects are universally present in every material, and significantly affect the physical properties and functions of materials [1–4]. In complex oxides, point defects have played a critical role in determining structural, electronic, optical, and electrochemical properties, especially via modifying the charge, spin, and orbital states of cations (e.g., transition metal ions). Recent advances in growth techniques for complex oxides have enabled the control of film stoichiometry to achieve highly pure materials with intrinsic bulk properties [5]. On the other hand, it has been also found that point defects can generate a broad spectrum of physical properties, including superconductivity [6], ferroelectricity [7–9], metal-insulator transitions [10], and emergent phenomena [11] in complex oxides. To date, it has been believed that most of the above emergent functions originate from oxygen vacancies, and the roles played by other intrinsic defects (e.g., cation vacancy and related defects) have been largely neglected.

SrTiO_3 is one of the most important and interesting complex oxides [12]. A pure, unstrained SrTiO_3 has a simple perovskite cubic structure at room temperature and is a nonmagnetic, paraelectric band insulator with an indirect band gap of ~ 3.2 eV [13]. Interestingly, an external perturbation, such as epitaxial strain and doping, has been employed to realize a wide range of physical properties and functions in SrTiO_3 . In addition to this intentional engineering, even small concentrations of unavoidable point defects can play a decisive role in the properties of SrTiO_3 . Strontium and oxygen vacancies have

been considered to be two dominant point defects in SrTiO_3 , because of their small formation energy [14,15]. While the Sr vacancy (V_{Sr}) can act to trap carriers and limit carrier mobilities [16], the oxygen vacancy (V_{O}) is considered to induce superconductivity [17] and *n*-type conductivity [18,19] in SrTiO_3 . In addition to V_{Sr} and V_{O} , recent works propose that an antisite Ti defect (Ti_{Sr}), where a Sr is replaced by a Ti atom [Fig. 1(a)], should also be intrinsically present and could lead to interesting and technologically important phenomena [7,9], such as visible light emission and ferroelectricity. However, it still remains elusive to unambiguously identify these point defects.

Cathodoluminescence (CL) spectroscopy has been one of the most successful techniques for characterizing defects in a material [20,21]. Besides near-band-gap and higher-lying energy transitions in semiconductors and insulators, luminescence at energies below the band gap arises from defect levels located in the band gap. In a simple material, the measured defect levels give rather straightforward evidence, from which we can identify point defects in the material. In contrast, a complicated structural and electronic reconstruction can occur due to point defects in complex oxides, which necessitates additional theoretical support. Although density functional theory (DFT) has been widely used to explore the electronic structure of complex oxides, its calculated band gap shows a quantitative mismatch with the experimental value [22,23]. This well-known band-gap problem has made it impossible to precisely compare the measured and calculated defect-induced optical transitions and identify the relevant point defects. Recently, a more reliable approach, that is, the Heyd, Scuseria, and Ernzerhof (HSE) hybrid functional [24,25], has been adopted in this field. The accuracy of HSE in predicting

*eom@engr.wisc.edu

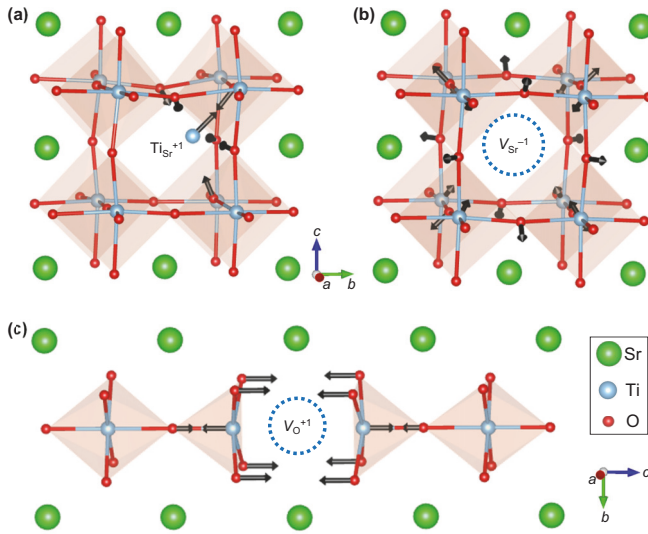


FIG. 1. Atomic structure distortions induced by a point defect. Calculated local atomic structures of SrTiO_3 with (a) $\text{Ti}_{\text{Sr}}^{+1}$, (b) $\text{V}_{\text{Sr}}^{-1}$, and (c) V_{O}^{+1} . The arrows indicate the directions of the atomic displacement away from the cubic symmetry due to the atomic reconstruction.

physical properties for SrTiO_3 has already been established [26,27], by reproducing not only the experimental band gap but also dielectric properties and the equilibrium crystal volume.

Here, using iterative feedback loops among atomic-layer- and stoichiometry-controlled thin-film epitaxy, hybrid density functional theory, and CL spectroscopy, we identify a functional point defect—Ti antisite (Ti_{Sr}) defect—in a complex oxide SrTiO_3 . Perovskite oxides usually have multiple intrinsic point defects, such as Ti_{Sr} , V_{Sr} , and V_{O} (Fig. 1), which can contribute to the emergence of functional properties in SrTiO_3 . Notably, those point defects not only can show distinct dielectric functions, but also can generate spectroscopically resolvable optical transitions. Therefore, by precisely calculating the defect-induced optical transitions and performing high-resolution CL measurements for the controlled thin films, we successfully identify all the measured sub-band-gap optical transitions from point defects and confirm the presence of a functional cationic defect, i.e., Ti_{Sr} , in SrTiO_3 .

II. EXPERIMENTAL AND THEORETICAL METHODS

Homoepitaxial SrTiO_3 thin films were grown on a (001) SrTiO_3 substrate using the pulsed laser deposition (PLD) method. Before deposition, low miscut ($<0.05^\circ$) SrTiO_3 substrates were treated with a buffered hydrofluoric acid etch and annealed in oxygen at 1050°C for 6 h to create atomically smooth single TiO_2 -terminated surfaces with unit-cell steps. A KrF excimer laser (248-nm) beam was focused on SrTiO_3 single-crystal targets to an energy density of $\sim 2.0\text{ J/cm}^2$ and pulsed at 5 Hz. SrTiO_3 films were grown at a substrate temperature of 750°C and oxygen partial pressures of 10 mTorr. The PLD system was equipped with high-pressure reflection high-energy electron diffraction (RHEED), which enabled atomic-layer-controlled growth and *in situ* monitoring during the growth [Fig. 2(a)]. After growth, the films were annealed

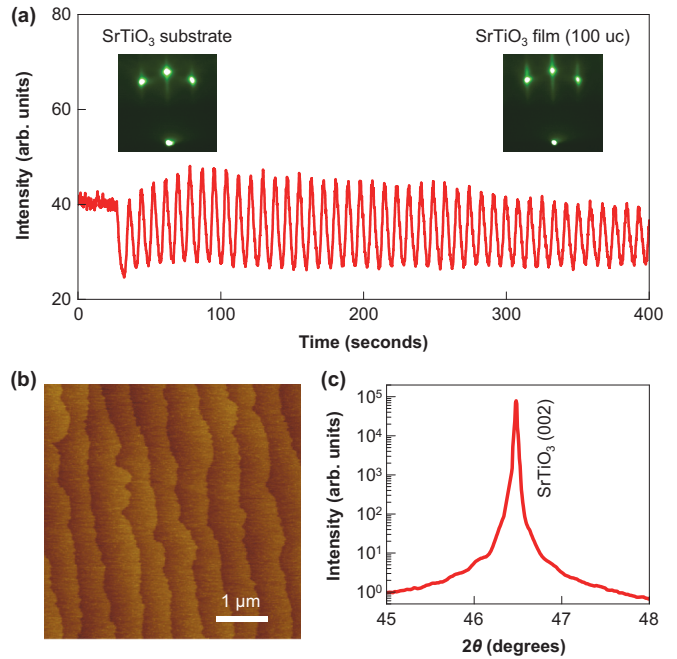


FIG. 2. Growth of homoepitaxial SrTiO_3 thin films. (a) RHEED intensity oscillations during growth of SrTiO_3 film on a SrTiO_3 (001) substrate. The insets show RHEED patterns of the SrTiO_3 substrate and 100-unit-cell-thick homoepitaxial SrTiO_3 film on SrTiO_3 . One unit cell corresponds to 0.3905 nm. (b) AFM image of 100-unit-cell-thick SrTiO_3 film, which shows the atomically smooth film surface. (c) XRD θ - 2θ curve around the SrTiO_3 (002) Bragg peak for 100-unit-cell-thick homoepitaxial SrTiO_3 film.

in 1 atm of oxygen during cooling. The crystal structure of the films was determined using a high-resolution four-circle x-ray diffraction (XRD) machine (Bruker D8 advance). The surface of the films was atomically smoothed with single unit-cell height steps measured by atomic force microscopy (AFM), as shown in Fig. 2(b).

For first-principles calculations, SrTiO_3 is modeled by a supercell of 160 atoms, constructed by the $2 \times 2 \times 2$ repetition of the 20-atom unit cell [28], which accommodates the octahedral rotation [29]. One defect is then generated within the 160-atom supercell for each of three types of defects of Ti_{Sr} , V_{Sr} , and V_{O} . For defects modeled in large supercells, the interaction between periodic images is small and can be neglected. Our first-principles calculations are based on the generalized Kohn-Sham density functional theory (DFT) with the screened hybrid functional HSE06 [24,25]. The structure optimizations have been performed by the CRYSTAL14 code package [30] that employs a linear combination (contraction) of localized Gaussian-type functions to represent the Bloch orbitals. The Hay-Wadt effective core potentials [31] have been adopted for Ti and Sr atoms, which replace only inner core orbitals with the effective potentials but orbitals for valence electrons are calculated self-consistently. The light oxygen atoms have been described by all-electron basis sets. The basis sets have been chosen following the literature [32]: O-8-411(1d)G, Ti-411(311d)G, and Sr-311(1d)G, where the numbers refer to the level of contraction. The integrations over the Brillouin zone were performed with a Γ -centered $2 \times 2 \times 2$ k -point

mesh. The self-consistent field convergence threshold on energy is set to be 10^{-8} Hartree. The structure is considered to be relaxed when 3×10^{-5} Hartree/Bohr in the root-mean-square values of forces and 1.2×10^{-4} Bohr in the root-mean-square values of atomic displacements are simultaneously achieved for atomic position and lattice constant optimizations, respectively. With the relaxed structures for each defect modeled in the SrTiO₃ supercell, we use DFT as implemented in the VASP [33] code package to identify the energies of the optical spectra. The formation energy of the Ti_{Sr} in a charge state q can be calculated by $E^f(\text{Ti}_{\text{Sr}}) = E_{\text{T}}(\text{Ti}_{\text{Sr}}) - E_{\text{T}}(\text{SrTiO}_3) - \mu_{\text{Sr}} + \mu_{\text{Ti}} + q(\varepsilon_{\text{VBM}} + E_{\text{F}}) + \Delta$, where $E_{\text{T}}(\text{SrTiO}_3)$ is the total energy of a perfect SrTiO₃ crystal system and $E_{\text{T}}(\text{Ti}_{\text{Sr}})$ is the total energy of the supercell containing a Ti_{Sr} in a charge state q . The atom X that is removed from the crystal is placed in a reservoir of energy μ_X , referenced to the total energy (per atom) of the standard phase. The reference of the Fermi level E_{F} is the energy at the valence-band maximum (VBM) ε_{VBM} of SrTiO₃ representing the energy of the electron reservoir. Δ is the charge-state-dependent finite-size correction [27]. To be consistent with previous work [34], we set $\mu_{\text{Ti}} = -4.0$ eV and $\mu_{\text{Sr}} = -3.4$ eV. Note that this choice does not affect the position of the thermodynamic transition levels, which correspond to the Fermi-level positions where formation energies of different charge states cross and the charge state of the defect changes.

Depth-resolved cathodoluminescence spectroscopy (DR-CLS) was performed using a Physical Electronics, Inc. (PHI) 110-10 glancing incidence electron gun operated with beam voltages from 0.5 to 4.5 kV and an emission current controlled to provide a constant power of 1 mW with varying voltages under ultrahigh vacuum (UHV) conditions. The emitted photons were collected by a CaF₂ lens in vacuum, and passed through a sapphire window port of the UHV chamber into an Oriel F-number matcher. The collected light was then dispersed through an Oriel MS260i monochromator using a grating with a 300-nm blaze into an Andor iDus OE charge coupled detector (CCD). To minimize charging by the incident electron beam, the sample was covered with a copper grid that was rinsed with acetone, methanol, isopropanol, and then de-ionized (DI) water prior to use. The electron gun's orientation prevented sample illumination by the filament glow. The normalized 1.8- and 2.1-eV peak intensities shown in Fig. 5(b) are defined as the intensity ratio between these CLS peaks and the near-band-edge peak at 3.6 eV [35].

III. RESULTS AND DISCUSSION

Figure 2(c) shows an XRD θ -2 θ scan of our sample around the SrTiO₃ (002) Bragg peak. The XRD peak position of the SrTiO₃ film was almost identical with that of the SrTiO₃ substrate, indicating that our SrTiO₃ film had a normal unit-cell volume (with a small expansion of $<0.1\%$) and was free of excessive point defects. Based on the measured lattice volume, we may expect that physical properties of the film would be quite similar to those of pure SrTiO₃ bulk. Our previous Raman spectroscopy measurements, however, revealed that our films are polar with the nonpolar-to-polar transition temperature at ~ 400 K [8,36], whereas pure SrTiO₃ bulk is nonpolar at every temperature. Furthermore, our electrical

measurements showed room-temperature ferroelectricity in our ultrathin SrTiO₃ homoepitaxial films [9]. Regarding the distinct Raman spectra of Sr- and Ti-deficient SrTiO₃ [36], we found our films to be Sr deficient, which was also confirmed by a chemical composition analysis such as wavelength dispersive x-ray spectroscopy [8]. This indicates the presence of a Sr-deficiency-related defect that generates ferroelectricity in our nominally stoichiometric SrTiO₃ films.

In the case of Sr-deficient SrTiO₃, our first-principles calculation shows that Ti_{Sr} is the only point defect that can generate polar distortion [9]. Figure 1 shows the calculated local atomic distortions at the vicinity of three representative intrinsic defects—Ti_{Sr}, V_O⁺¹, and V_{Sr}⁻¹—modeled in a large SrTiO₃ supercell. Among these three types of defects, Ti_{Sr} is only the point defect that breaks the inversion symmetry, generating a large electric dipole. The broken inversion symmetry is facilitated by an electronic reconstruction induced by Ti_{Sr}. The total energy is significantly lowered by the electronic hybridization between the Ti-3d states and the O-2p electronic states. Atomic reconstructions occur consequently, which can be clearly seen by the Ti_{Sr} forming relatively stronger Ti-O bonds with six of the oxygen atoms, while moving away from the other six oxygen atoms in its first coordination shell, as presented in Fig. 1(a). Such a drastic atomic reconstruction generates an electric dipole around 10 e \AA in our first-principles calculations, which is significantly larger than that in a conventional ferroelectric BaTiO₃ of 1.3 e \AA .

On the other hand, due to the featureless nature of the electronic structure of charged vacancies, a V_{Sr}⁻¹ or V_O⁺¹ defect does not introduce any abrupt electronic reconstruction in SrTiO₃. The atoms surrounding these charged vacancies respond to an electrostatic interaction from the defect. The resulting local atomic structures are distorted away from the original cubic symmetry, however, rather isotopically. Not surprisingly, the inversion symmetries are preserved and no local electric dipole is generated in both types of vacancies, as seen in Figs. 2(b) and 2(c). It should be noted that we theoretically examined all the possible point defects and their clusters in the case of Sr-deficient SrTiO₃, and found that only the Ti_{Sr} induces a stable switchable polarization [9], a prerequisite for ferroelectricity.

Interestingly, our calculation also revealed that Ti_{Sr} induces local oxygen-octahedral tilts, as well as local polarization (Fig. 1). While these octahedral tilts can mainly change the local crystal shape, the overall crystal volume might remain almost preserved. The crystal volume change in SrTiO₃ with Ti_{Sr} was calculated as small as $\sim 0.3\%$, compared to that of stoichiometric SrTiO₃, and it will be even smaller when the calculated cell size is sufficiently large. Notably, the crystal volume was decreased by Ti_{Sr}, rather than being increased. Therefore, according to our calculations, Ti_{Sr} can generate polar distortion, but does not induce an excessive crystal volume change, consistent with our XRD, Raman, and electrical measurements.

For the next step, we theoretically examined the optical transition from Ti_{Sr} for checking if it is optically detectable. Assuming that Ti_{Sr} initially exists in a +1 charge state (i.e., Ti_{Sr}⁺¹), the localized electron in the defect state can recombine with a hole in the valence band, the latter of which is generated by the electron-hole excitation process of the experiment. Following the above process, the Ti_{Sr}⁺¹ is converted to a

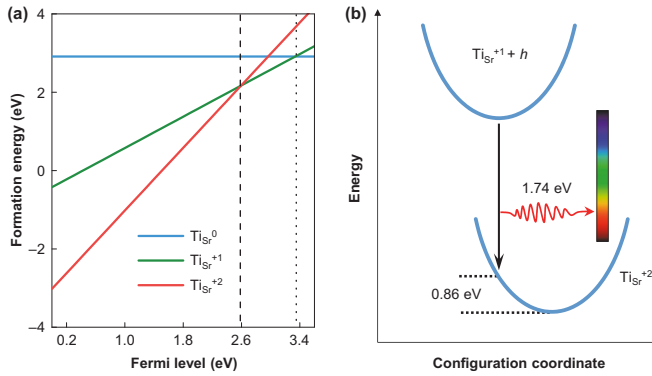


FIG. 3. Microscopic mechanism for luminescence process by Ti_{Sr} . (a) Formation energy of Ti_{Sr} defect of 0, +1, and +2 charge states. (b) Schematic plot of the configuration coordinate diagram for the optical process $\text{Ti}_{\text{Sr}}^{+1} + h \rightarrow \text{Ti}_{\text{Sr}}^{+2}$, which emits photons.

+2 charge state (i.e., $\text{Ti}_{\text{Sr}}^{+2}$), as described by $\text{Ti}_{\text{Sr}}^{+1} + h \rightarrow \text{Ti}_{\text{Sr}}^{+2}$, emitting photons simultaneously. When the Fermi level is below 2.6 eV above the VBM, there is a possibility that Ti_{Sr} mainly exists in the +2 charge state. In this case, the electron can be excited from the valence band to the empty defect state during optical excitation and generate a +1 charge state, thus allowing the same optical emission process $\text{Ti}_{\text{Sr}}^{+1} + h \rightarrow \text{Ti}_{\text{Sr}}^{+2}$. Theoretically, the above optical spectra can be determined by the thermodynamic transition level as well as the correction considering the Stokes shifts. As shown in Fig. 3(a), the thermodynamic transition level between $\text{Ti}_{\text{Sr}}^{+2}$ and $\text{Ti}_{\text{Sr}}^{+1}$ states is revealed to be 2.6 eV above the VBM from our first-principles calculations based on hybrid density functional theory. Compared with the generalized gradient approximation (GGA + U) results with the *ad hoc* band-gap correction in Ref. [7], the (2+/+) transition level for the Ti

antisite defect is shifted from 2.13 eV above the VBM in Ref. [7] to 2.6 eV above the VBM by our HSE calculations. We believe that HSE provides a more reliable description of the electronic structure in order to determine the transition levels and corresponding optical signatures. The characteristic time of lattice relaxation is much longer than that of the electron-hole excitations. Therefore, the local atomic structure can be assumed to be intact during the optical process according to the Frank-Condon principle. This physical principle allows us to predict the optical transition associated with Ti_{Sr} to be at 1.74 eV, with the computed Stokes shift of 0.86 eV, as schematically shown by our configuration coordinate diagram in Fig. 3(b). By the same token, the optical transitions at 2.80 and 2.03 eV have been predicted to be associated with an oxygen vacancy of the +1 charge state (i.e., V_O^{+1}) and Sr vacancy of the -1 charge state (i.e., $\text{V}_{\text{Sr}}^{-1}$), respectively, which are also consistent with recent calculations [34].

In order to measure those point-defect-induced optical transitions, we carried out the CL measurements for nominally stoichiometric SrTiO_3 and slightly Sr-deficient $\text{Sr}_{0.99}\text{TiO}_3$ thin films, as shown in Fig. 4(a). Importantly, we were able to achieve a high depth resolution by a differential technique, subtracting suitably normalized spectra acquired at a lower energy from slightly higher-energy spectra [37]. The measured CL data exhibit the spectral fine structures with multiple peaks at ~ 1.6 , ~ 1.8 , ~ 2.1 , and ~ 2.9 eV, which are more obvious in $\text{Sr}_{0.99}\text{TiO}_3$ [lower panel in Fig. 4(a)], along with broad signals at 2.3–2.6 eV due to V_O -related defects [37]. Other strong peaks at ~ 3.6 and ~ 4.1 eV correspond to the direct-band-gap emission and above-band-gap emission from $\text{Ti} t_{2g}$ orbitals [35], respectively. All these measured peak energies are in excellent agreement with our theoretical calculations. Figure 4(b) illustrates the optical transitions, either predicted from first-principles calculations or taken from the literature [38], showing 1.60, 1.74, 2.03, and 2.80 eV optical transitions

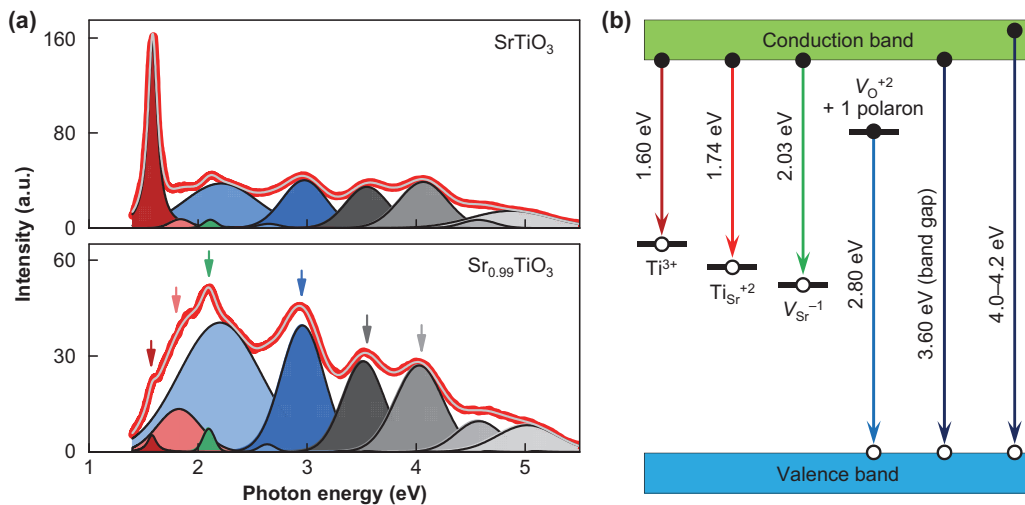


FIG. 4. Point-defect-induced fine structures in the cathodoluminescence (CL) spectra of SrTiO_3 . (a) CL spectra for 24-unit-cell-thick homoepitaxial SrTiO_3 (upper panel) and $\text{Sr}_{0.99}\text{TiO}_3$ (lower panel) films. The CL spectra are fitted with nine Gaussian curves (with the centers at ~ 1.8 , ~ 2.1 , ~ 2.3 , ~ 2.6 , ~ 2.9 , ~ 3.6 , ~ 4.1 , ~ 4.5 , and ~ 4.9 eV) and one Lorentzian curve (with the center at ~ 1.6 eV). Six peaks at ~ 1.6 , ~ 1.8 , ~ 2.1 , ~ 2.9 , ~ 3.6 , and ~ 4.1 are denoted by arrows. Red and gray solid lines indicate experimental and fitted data, respectively. (b) Schematics of luminescence processes. The luminescence by Ti_{Sr} , V_{Sr} , and V_O is predicted from hybrid density functional theory, and the one by Ti^{3+} is from Ref. [38].

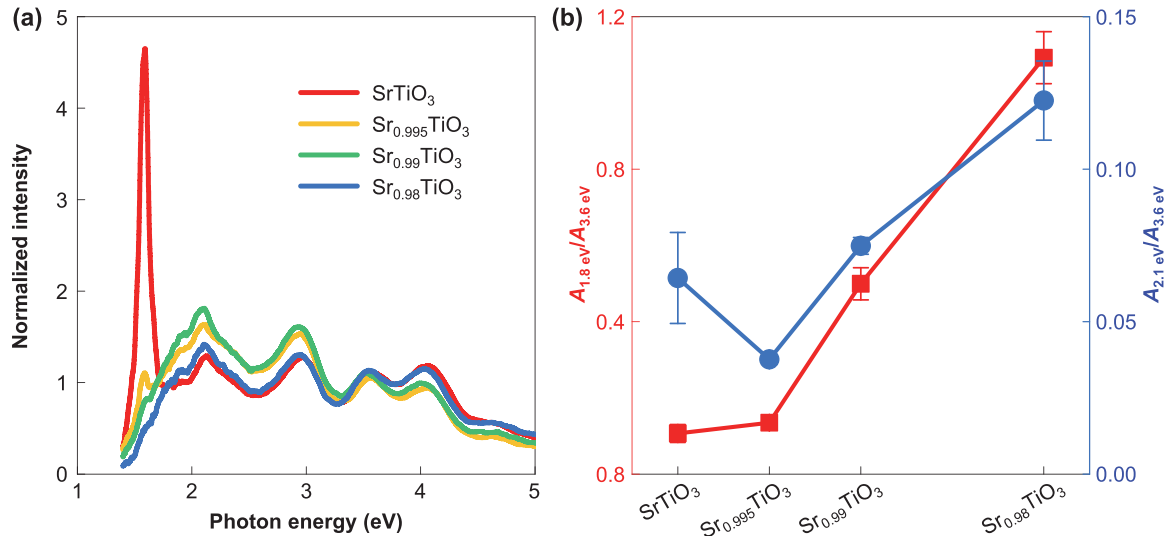


FIG. 5. Identification of point defects by the controlled Sr deficiency in SrTiO₃. (a) CL spectra for 24-unit-cell-thick homoepitaxial SrTiO₃, Sr_{0.995}TiO₃, Sr_{0.99}TiO₃, and Sr_{0.98}TiO₃ films. We normalize the peak intensity with that of the 3.6-eV CL peak (corresponding to the direct band gap). (b) Areas under the 1.8-eV (red squares) and 2.1-eV (blue circles) CL peaks, normalized with that under the 3.6-eV CL peak, as a function of Sr deficiency.

by Ti³⁺, Ti_{Sr}⁺¹, V_{Sr}⁻¹, and V_O⁺², respectively. Therefore, based on this quantitative agreement, as well as one-to-one correspondence, between theoretical and experimental data, we could effectively evidence the presence of several point defects, including the functional Ti_{Sr}, in SrTiO₃ thin films.

Note that positively charged Ti_{Sr} can couple with negatively charged V_O through the attractive Coulomb interaction to form defect complexes. However, this does not rule out the existence of isolated defects and their corresponding optical peaks. Furthermore, as studied in Ref. [7], the Ti_{Sr}-V_O complexes are predicted to exhibit optical absorption and emission peaks at energies that are close to what are induced by the isolated Ti_{Sr}. This supports the notion that the optical transition at \sim 1.8 eV could originate from the Ti_{Sr}-related defect, not depending on whether it is isolated or forms a complex with V_O.

Defect energy levels are often located closely, making it challenging to assign the defects unambiguously, only by using the theory and spectroscopic measurement. For example, we found that in nominally stoichiometric SrTiO₃ films [upper panel in Fig. 4(a)], the 1.6 eV CL peak by Ti³⁺ is dominant and can mask the signals from other point defects, especially from Ti_{Sr} at \sim 1.8 eV. Although pure SrTiO₃ is an insulator, oxygen vacancies can introduce free electrons, resulting in Ti³⁺ neighboring sites and associated luminescence at \sim 1.6 eV [38]. Precise control of the oxygen vacancy concentration in SrTiO₃ is difficult, resulting in large variations of both the 1.6-eV Ti³⁺-related and 2.9 eV V_O-related CL peaks. However, deposition of SrTiO₃ with carefully controlled stoichiometry could permit us to vary the concentration of these defects, demonstrating our ability to systematically tune the 1.6-eV and other defect-mediated CL peaks in SrTiO₃. This systematics in CL spectra would allow for more reliable defect assignment.

For such a systematic study, we performed CL measurements for Sr_{1-x}TiO₃ thin films with the controlled Sr deficiency. We prepared four systematic Sr_{1-x}TiO₃ samples ($x \sim 0.00, 0.005, 0.01$, and 0.02) [28], using the same SrTiO₃

substrate that was cut into smaller pieces for the film growth. Importantly, based on our DFT calculations [28], we controlled the Sr deficiency in our samples to be below $x = 0.06$, where we could treat a defect as being isolated. In contrast to donor-like V_O, V_{Sr} can act as an electron acceptor, so it can suppress the formation of Ti³⁺. Figure 5(a) shows the CL spectra for SrTiO₃, Sr_{0.995}TiO₃, Sr_{0.99}TiO₃, and Sr_{0.98}TiO₃, where the data of SrTiO₃ and Sr_{0.99}TiO₃ are identical to those in Fig. 4(a). With the increase of Sr deficiency, the 1.6-eV CL peak becomes suppressed, whereas the 1.8- and 2.1-eV CL peaks become enhanced. We quantitatively analyzed the enhancement of 1.8- and 2.1-eV CL peaks for larger Sr deficiency [Fig. 5(b)], by normalizing their peak area with that of the band-gap emission at \sim 3.6 eV. While Sr_{0.995}TiO₃ shows a slightly decreased 2.1-eV peak area, possibly due to filling of any A-site vacancies with Ti, both 1.8- and 2.1-eV peaks show a general enhancement with an increased Sr deficiency. This systematic change is consistent with our understanding that 1.6-, 1.8-, and 2.1-eV CL peaks come from Ti³⁺, Ti_{Sr}, and V_{Sr}, respectively.

IV. CONCLUSION

In summary, we have identified a functional cationic defect, i.e., Ti_{Sr}, in SrTiO₃, using a combination of atomic-layer- and stoichiometry-controlled thin-film epitaxy, hybrid density functional calculation, and high-resolution CL measurement. All the measured sub-band-gap luminescence could be assigned to the optical transitions from point defects such as Ti_{Sr}, with excellent quantitative agreement with theoretical predictions. We also demonstrated that spectral fine structures in the defect-induced luminescence could be systematically tuned, for example, by theory-guided, intentional control of cationic stoichiometry. Our study allows a better microscopic understanding of how a point defect contributes to the optical transitions, and guides us to effectively identify the point defect in complex oxides. Our methodology described here is not

limited to SrTiO_3 , but will be generally applicable to other complex oxides and materials for identifying and utilizing functional point defects. It should be also of great interest to directly visualize the functional cationic defects in complex oxides, e.g., by using transmission electron microscopy [39].

ACKNOWLEDGMENTS

This work at University of Wisconsin-Madison (Synthesis and structural characterization) was supported by funding from

the DOE Office of Basic Energy Sciences under Award No. DE-FG02-06ER46327. The work at Temple University was partially supported as part of the Center for the Computational Design of Functional Layered Materials, an Energy Frontier Research Center funded by the U.S. Department of Energy, Office of Science, Basic Energy Sciences under Award No. DE-SC0012575 (H.W. and X.W. carried out the defect calculations and analysis). B.A.N., T.A., and L.J.B. were supported by National Science Foundation Award No. DMR-1305193.

D.L., H.W., and B.A.N. contributed equally to this work.

- [1] S. Aggarwal and R. Ramesh, Point defect chemistry of metal oxide heterostructures, *Annu. Rev. Mater. Sci.* **28**, 463 (1998).
- [2] H. L. Tuller and S. R. Bishop, Point defects in oxides: Tailoring materials through defect engineering, *Annu. Rev. Mater. Res.* **41**, 369 (2011).
- [3] N. Poccia, M. Fratini, A. Ricci, G. Campi, L. Barba, A. Vittorini-Orgeas, G. Bianconi, G. Aeppli, and A. Bianconi, Evolution and control of oxygen order in a cuprate superconductor, *Nat. Mater.* **10**, 733 (2011).
- [4] S. V. Kalinin and N. A. Spaldin, Functional ion defects in transition metal oxides, *Science* **341**, 858 (2013).
- [5] D. G. Schlom, Perspective: Oxide molecular-beam epitaxy rocks!, *APL Mater.* **3**, 062403 (2015).
- [6] P. A. Lee, N. Nagaosa, and X.-G. Wen, Doping a Mott Insulator: Physics of High-Temperature Superconductivity, *Rev. Mod. Phys.* **78**, 17 (2006).
- [7] M. Choi, F. Oba, and I. Tanaka, Role of Ti Antisitelike Defects in SrTiO_3 , *Phys. Rev. Lett.* **103**, 185502 (2009).
- [8] H. W. Jang *et al.*, Ferroelectricity in Strain-Free SrTiO_3 Thin Films, *Phys. Rev. Lett.* **104**, 197601 (2010).
- [9] D. Lee *et al.*, Emergence of room-temperature ferroelectricity at reduced dimensions, *Science* **349**, 1314 (2015).
- [10] E. Abrahams and G. Kotliar, The metal-insulator transition in correlated disordered systems, *Science* **274**, 1853 (1996).
- [11] E. Miranda and V. Dobrosavljevic, Disorder-driven non-Fermi liquid behaviour of correlated electrons, *Rep. Prog. Phys.* **68**, 2337 (2005).
- [12] K. A. Müller and H. Burkard, SrTiO_3 : An intrinsic quantum paraelectric below 4 K, *Phys. Rev. B* **19**, 3593 (1979).
- [13] M. Cardona, Optical properties and band structure of SrTiO_3 and BaTiO_3 , *Phys. Rev.* **140**, A651 (1965).
- [14] K. R. Udayakumar and A. N. Cormack, Non-stoichiometry in alkaline earth excess alkaline earth titanate, *J. Phys. Chem. Solids* **50**, 55 (1989).
- [15] B. Liu, V. R. Cooper, H. Xu, H. Xiao, Y. Xhang, and W. J. Weber, Composition dependent intrinsic defect structures in SrTiO_3 , *Phys. Chem. Chem. Solids* **16**, 15590 (2014).
- [16] Y. Kozuka, Y. Hikita, C. Bell, and H. Y. Hwang, Dramatic mobility enhancements in doped SrTiO_3 thin films by defect management, *Appl. Phys. Lett.* **97**, 012107 (2010).
- [17] J. Schooley, W. Hosler, and M. Cohen, Superconductivity in Semiconducting SrTiO_3 , *Phys. Rev. Lett.* **12**, 474 (1964).
- [18] O. N. Tufte and P. W. Chapman, Electron mobility in semiconducting strontium titanate, *Phys. Rev.* **155**, 796 (1967).
- [19] A. Ohtomo and H. Y. Hwang, Growth mode control of the free carrier density in $\text{SrTiO}_{3-\delta}$ films, *J. Appl. Phys.* **102**, 083704 (2007).
- [20] R. E. Viturro, M. L. Slade, and L. J. Brillson, Optical-Emission Properties of Interface States for Metals on III-V Semiconductor Compounds, *Phys. Rev. Lett.* **57**, 487 (1986).
- [21] L. J. Brillson, Interface bonding, chemical reactions, and defect formation at metal-semiconductor interfaces, *J. Vac. Sci. Technol. A* **25**, 943 (2007).
- [22] J. P. Perdew and Y. Wang, Accurate and simple analytic representation of the electron-gas correlation energy, *Phys. Rev. B* **45**, 13244 (1992).
- [23] P. Deak, A. Gali, B. Aradi, and T. Frauenheim, Accurate gap levels and their role in the reliability of other calculated defect properties, *Phys. Status Solidi B* **248**, 790 (2011).
- [24] J. Heyd, G. E. Scuseria, and M. Ernzerhof, Hybrid functionals based on a screened Coulomb potential, *J. Chem. Phys.* **118**, 8207 (2003).
- [25] J. Heyd, G. F. Scuseria, and M. Ernzerhof, Hybrid functionals based on a screened Coulomb potential, *J. Chem. Phys.* **124**, 219906 (2006).
- [26] R. Wahl, D. Vogtenhuber, and G. Kresse, SrTiO_3 and BaTiO_3 revisited using the projector augmented wave method: Performance of hybrid and semilocal functionals, *Phys. Rev. B* **78**, 104116 (2008).
- [27] C. Freysoldt, J. Neugebauer, and C. G. Van de Walle, Fully *Ab Initio* Finite-Size Corrections for Charged-Defect Supercell Calculations, *Phys. Rev. Lett.* **102**, 016402 (2009).
- [28] See Supplemental Material at <http://link.aps.org/supplemental/10.1103/PhysRevMaterials.2.060403> for (i) growth of Sr-deficiency-controlled thin films, (ii) finite-size correction scheme for defect simulations, and (iii) fitting of CL spectra.
- [29] H. Wang, J. Wen, D. J. Miller, Q. Zhou, M. Chen, H. N. Lee, K. M. Rabe, and X. Wu, Stabilization of Highly Polar BiFeO_3 -like Structure: A New Interface Design Route for Enhanced Ferroelectricity in Artificial Perovskite Superlattices, *Phys. Rev. X* **6**, 011027 (2016).
- [30] R. Dovesi *et al.*, CRYSTAL14: A program for the *ab initio* investigation of crystalline solids, *Int. J. Quantum Chem.* **114**, 1287 (2014).
- [31] P. J. Hay and W. R. Wadt, *Ab initio* effective core potentials for molecular calculations. Potentials for the transition metal atoms Sc to Hg, *J. Chem. Phys.* **82**, 270 (1984).
- [32] S. Piskunov, E. Heifets, R. I. Egлитис, and G. Borstel, Bulk properties and electronic structure of SrTiO_3 , BaTiO_3 , PbTiO_3

perovskites: An *ab Initio* HF/DFT study, *Comput. Mater. Sci.* **29**, 165 (2004).

[33] G. Kresse and J. Furthmuller, Efficiency of *ab-initio* total energy calculations for metals and semiconductors using a plane-wave basis set, *Comput. Mater. Sci.* **6**, 15 (1996).

[34] A. Janotti, J. B. Varley, M. Choi, and C. G. Van de Walle, Vacancies and small polarons in SrTiO₃, *Phys. Rev. B* **90**, 085202 (2014).

[35] K. van Benthem and C. Elsässer, Bulk electronic structure of SrTiO₃: Experiment and theory, *J. Appl. Phys.* **90**, 6156 (2001).

[36] D. A. Tenne, A. K. Farrar, C. M. Brooks, T. Heeg, J. Schubert, H. W. Jang, C. W. Bark, C. M. Folkman, C. B. Eom, and D. G. Schlom, Ferroelectricity in nonstoichiometric SrTiO₃ films studied by ultraviolet Raman spectroscopy, *Appl. Phys. Lett.* **97**, 142901 (2010).

[37] T. J. Asel, H. Gao, T. J. Heinl, D. Adkins, P. M. Woodward, J. Hoffman, A. Bhattacharya, and L. J. Brillson, Near-nanoscale-resolved energy band structure of LaNiO₃/La_{2/3}Sr_{1/3}MnO₃/SrTiO₃ heterostructures and their interfaces, *J. Vac. Sci. Technol. B* **33**, 04E103 (2015).

[38] J. Zhang, D. Doutt, T. Merz, J. Chakhalian, M. Kareev, J. Liu, and L. J. Brillson, Depth-resolved subsurface defects in chemically etched SrTiO₃, *Appl. Phys. Lett.* **94**, 092904 (2009).

[39] H. Kim, J. Y. Zhang, S. Raghavan, and S. Stemmer, Direct Observation of Sr Vacancies in SrTiO₃ by Quantitative Scanning Transmission Electron Microscopy, *Phys. Rev. X* **6**, 041063 (2016).